

Ianko Chtereov, Isaac Boxx, Effect of Hydrogen Enrichment on the Dynamics of a Lean Technically Premixed Elevated Pressure Flame, *Combust. Flame* 225 (2021) 149-159.

The original publication is available at www.elsevier.com

<https://doi.org/10.1016/j.combustflame.2020.10.033>

© 2020. This manuscript version is made available under the CC-BY-NC-ND

4.0 license <http://creativecommons.org/licenses/by-nc-nd/4.0/>

Effect of Hydrogen Enrichment on the Dynamics of a Lean Technically Premixed Elevated Pressure Flame

Authors: I. Chterev¹, I. Boxx¹

Affiliations:

Institut für Verbrennungstechnik, Deutsches Zentrum für Luft- und Raumfahrt (DLR),
70569 Stuttgart, DE

Corresponding Author:

Dr. Ianko Chterev
Deutsches Zentrum für Luft- und Raumfahrt e.V.
Institut für Verbrennungstechnik
Pfaffenwaldring 38-40
70569 Stuttgart
Germany

Tel.: +49 711 6862-8858

ianko.chtere@dlr.de

Abstract

The heat release distribution, combustion instability characteristics and flow dynamics of lean swirl-stabilized flames of hydrogen enriched natural gas were studied using time-resolved (10 kHz) stereo PIV, OH* chemiluminescence imaging and acoustic pressure measurements. The technically premixed gas turbine model combustor was operated at elevated pressure up to 5bar with preheated air. The H₂ volume fraction in the fuel was varied up to 50%. An M-shaped aerodynamically stabilized flame persisted at 1bar up to low H₂ enrichment ratios. Increasing H₂ enrichment caused the M-flame to first transition to a bistable flame then to a shear layer stabilized V-flame. Increasing pressure and H₂ enrichment both decreased the flame length. The combustion instability frequency and thermoacoustic amplitude varied and were mapped across operating conditions. The effect of H₂ enrichment on the thermoacoustic amplitude was explained by examining the convective coupling between the Helmholtz acoustics and heat release. H₂ enrichment was shown to increase the phase delay between the pressure and heat release by decreasing the pressure wave travel times in the plenum and swirler sections of the burner and by decreasing the flame length while simultaneously increasing the pressure wave speed within the burner. Thus H₂ enrichment increased the thermoacoustic amplitude when the phase delay at the initial condition was negative, and decreased it when the initial phase delay was positive. Flow dynamics were studied by characterizing the precessing vortex core frequency and energy. The PVC structure existed across all conditions, and its frequency reduced to a different Strouhal number for the M-flame and V-flame. H₂ enrichment consistently slightly decreased the PVC energy.

1. Introduction

Combustion of hydrogen is increasingly relevant to industry and power generation as a means of chemical storage via electrolysis of electrical energy from renewable sources such as solar and wind, and as a means to reduce carbon emissions. One strategy for implementing H₂ fuel in industrial gas turbines is through H₂ enrichment of natural gas (NG) in existing or modified hardware. The different chemical properties of H₂ present significant combustor design challenges. Namely, the higher flame speed and higher flame temperature imply that the flame will stabilize differently, have a different length, and exhibit different dynamics. These different combustion physics affect combustor performance parameters such as hardware heat loading, combustor exit pattern factor, ignition and blow-off, combustion instability limits, and pollutant

and noise emissions. H₂-enriched NG combustion also has the potential to reduce pollutant emissions (specifically NO_x) by allowing operation at leaner fuel/air equivalence ratios (ER).

Premixed H₂-enriched flame stability and emissions have been studied extensively with laboratory model combustors [1-7]. Researchers observed that H₂ enrichment lowers the extinction ER, changes the extinction dynamics, and can change the flame shape in flow fields with multiple flame stabilization locations. Thermoacoustic oscillations in combustors or combustion instabilities occur when the combustor acoustics couple to the heat release. High amplitudes of these oscillations can cause immediate damage or shorten hardware life through increased thermal and mechanical stresses, and are, therefore, highly undesirable. Combustion instability limits and the spectral characteristics of thermoacoustic fluctuations are also important in the design of quiet gas turbines. H₂ enrichment has been observed to change the combustion instability limits and dynamics by altering the heat release distribution and fluid dynamic properties [2,5]. By modifying the flame length, flame shape, and flow topology, combustor pressure and H₂ enrichment can change the thermoacoustic frequency and amplitude, as well as the active thermoacoustic modes.

Swirling flows are subject to hydrodynamic instabilities such as helical vortices (HV) in the shear layers and a precessing vortex core (PVC) in the inner recirculation zone (IRZ) [8-10]. PVC is a global hydrodynamic instability mode, the formation of which is closely related to the local transition from convective to absolute instability in the wavemaker region [11-12]. Manoharan et al. [13] formally show using stability theory and experiments that the PVC onset as a self-excited instability is triggered by perturbations along the flow axis generated by vortex breakdown. Interactions between the center body wake and the vortex breakdown bubble can also affect PVC onset. For example Arnab et al. [14] demonstrate that PVC forms if the stagnation point of the vortex breakdown bubble is downstream of the centerbody wake. The PVC and associated HVs affect the flame stabilization and heat release by creating instantaneous stagnation points and distorting the flame [15-16]. Since the PVC and HV are sensitive to density field non-homogeneities [17-18], they are expected to be sensitive to H₂ enrichment.

Most of the available data on combustors with H₂-enriched NG are at atmospheric pressure. To closer approach real engine power density, temperature and Reynolds number (Re), elevated pressure experiments with preheated air are necessary. Such experiments are expensive and technically complex, and therefore,

uncommon. This study aims to examine the effects of H₂ enrichment of NG in a gas turbine model combustor with preheated air and at elevated pressure combined using detailed optical diagnostics. The burner used is based on the PRECCINSTA design, which has been studied widely experimentally [18-19] and computationally [20-21] mostly at atmospheric pressure, but also at elevated pressure [22-23]. The fuel is mixed with preheated air in the swirler. The heat release distribution, combustion instability characteristics and flow dynamics are studied using simultaneous, time-resolved (10 kHz) stereo PIV, OH* chemiluminescence imaging and acoustic measurements. The objective of this work is two-fold. First, operation of the H₂-enriched NG (up to 50% per volume) swirl burner at pressures up to 5bar is demonstrated. The operational space is mapped out by detailing changes to the heat release distribution, combustion instability and PVC/HV characteristics. Second, the effects of pressure and H₂ enrichment on thermoacoustic characteristics and stability limits are examined by considering the thermoacoustic mechanism.

Previous studies [18-21] have established that the main thermoacoustic mechanism for this geometry is convective coupling between the Helmholtz modes of the plenum, swirler and combustor system, and the heat release via mass flow fluctuations. The air supply to the plenum has high acoustic impedance but the pressure in the large plenum volume responds to the acoustics resulting in air mass flow fluctuations. ER fluctuations due to the fuel being injected in the swirler are an additional [18-19] but not necessary [26] coupling mechanism, and the HV associated with a PVC has been shown [18,24-25] to modify the heat release distribution. In this work, the effect of H₂ on the combustion instability frequency and amplitude is examined in detail by considering the convective coupling between the acoustics and heat release.

A PVC accompanied by a single frequency-locked HV has been observed in previous studies of the PRECCINSTA burner at atmospheric [15,24-25] and elevated pressures [22-23]. The PVC distorts the inner recirculation zone flow [18,23-25], and the helical vortices affect flame stabilization by providing stagnation points and rolling up the flame. The HV also modifies the heat release by increasing flame surface area [18,23-25]. In this paper we will refer to the PVC and associated HV as the PVC structure. This work describes the effect of H₂ enrichment at elevated pressure on the PVC frequency and strength.

2. Experiment

2.1. Gas turbine model combustor

A technically premixed gas turbine model combustor installed in the High Pressure Optical test rig (HIPOT) at DLR-Stuttgart, shown in Figure 1 [22-23], was operated at elevated pressure. By technically premixed, we mean that the reactants are premixed in a manner approximating that used in a technical combustion system. Preheated air enters the plenum and passes through a swirl generator with 12 radial channels. Hydrogen-enriched natural gas (H₂-NG) is injected through 1mm orifices in the swirl channels. The NG composition was logged in real time using a gas chromatograph (Agilent 490 Micro GC), and had a composition of 93% CH₄, 4% C₂H₆, 1.5% N₂, 1% CO₂, and 0.5% heavy hydrocarbons. The swirling reactant flow enters the combustion chamber through a nozzle with an exit diameter of $D_0 = 27.85\text{mm}$, passing around a conical inner centerbody. The centerbody tip is flush with the combustor dump plane. The chamber has a square cross-section of $80 \times 80\text{mm}^2$ and a total length of 200mm. Optical access to the flame is provided through all four walls of the combustion chamber using a series of fused silica windows. The combustor exit is a contracting duct with 18mm inner diameter, D_e . A water-cooled throttle valve is used to control the chamber pressure.

The inner test section windows are back-face air-cooled and all other test rig hardware is water-cooled. The air mass flow rate to the experiment is measured with a thermal mass flow sensing flow meter (Bronkhorst F-106CI-RGD-03-V), while the fuel mass flow rates are measured with Coriolis flow meters (NG: Bronkhorst M14-RGD-33-0-S, H₂: Bronkhorst F-116AI-RBD-55V). As reported by the manufacturer, the measurement accuracy is $\pm 1.0\%$ of full scale ($\pm 2.2\text{g/s}$) for air, and $\pm 0.5\%$ of reading for fuel. The repeatability of the flow measurement is $\pm 0.2\%$ of reading for air, and $\pm 0.05\%$ of reading for fuel.

All operating conditions, including pressures, temperatures, and air/fuel/water mass flow rates were monitored and recorded at a 1Hz interval.

2.2. Detailed time-resolved diagnostics

10 kHz stereo PIV, OH* chemiluminescence, and acoustic pressure measurements are acquired simultaneously. The optical setup is illustrated in Figure 2 [22-23].

2.2.1. Stereo PIV

A dual-cavity diode-pumped solid-state (DPSS) Nd:YAG laser (Edgewave IS611-DE) was Q-switched and frequency-doubled to produce 2.6mJ 532nm pulse pairs (temporally separated by $\Delta t = 3\mu\text{s}$) at a repetition rate of 10kHz. The laser beam was formed into a 50mm wide collimated sheet using a cylindrical telescope and focused to a $\sim 1\text{mm}$ waist using a third cylindrical lens. The flow was seeded with titanium dioxide particles (TiO_2) of $1\mu\text{m}$ nominal diameter, using a fluidized bed seeder. Metered unheated air fed the particle seeding system and was introduced at the inlet plenum. This unheated flow was maintained when not seeding by diverting it through a bypass circuit. Seed air flow rate was about 7-10% of the total combustor air. To reduce clumping the seed particles were dried in a 250°C oven for 24 hours and kept outside of the oven for no longer than 4 hours, including run time.

Mie scattering from the particles was collected by two high-speed CMOS cameras (Phantom v1212) through 200mm, f/4.0 objective lenses (Nikon Nikkor IF-ED Micro) in a stereo configuration 35° off-normal, equipped with Scheimpflug adapters. A narrowband interference filter (532nm, 3nm FWHM) was used to reject flame luminosity. 10000 dual-frame images per run were recorded at $640 \times 800 \text{ pixel}^2$ resolution. The field of view (FOV) within the combustor was $\pm 30\text{mm}$ in transverse and 50mm in the axial direction, and is indicated in Figure 1. A pixel corresponds to about $75\mu\text{m}$. The images were registered using a dot target and processed to extract velocity vectors using a commercial multi-pass adaptive window offset cross-correlation software package (LaVision DaVis 8). The final interrogation window resolution and overlap were 16×16 pixels and 50%. This corresponds to an interrogation window size of 1.30mm and vector spacing of 0.65mm. Measurement uncertainty in velocity based on correlation statistics (computed in DaVis) is about 1% in the low velocity recirculation zones (see Figure 1), about 2.5% in the high turbulence intensity shear layers, and about 0.5% in the annular jet.

2.2.2. OH* chemiluminescence

OH* chemiluminescence (CL) is a common and reliable marker for heat release in lean, premixed hydrocarbon flames [27-29] and has been used extensively to characterize the release dynamics in the PRECCINSTA burner [18-19, 22-26]. OH* CL was imaged with a high-speed CMOS camera (LaVision HSS8) equipped with an external, lens-coupled image intensifier (LaVision IRO). The OH* CL signal was

collected with a 45mm, $f/1.8$ objective (Cerco) through a high transmission ($>80\%$ at 310nm) bandpass interference filter. The intensifier gate time was $20\mu\text{s}$. 10000 CL images were acquired per run at 640×640 pixel² image size. The FOV is indicated in Figure 1. The combustor was imaged fully transversely and for about 75mm in the axial direction, resulting in a pixel corresponding to about $130\mu\text{m}$. Dark background subtraction and a uniform white field correction were applied.

2.3. Acoustic pressure

Pressure was measured in the upstream plenum, combustion chamber, and downstream section with amplitude and phase calibrated probes equipped with high frequency piezo-resistive pressure transducers (Kistler 4043A with a 4603A amplifier). The signals were recorded simultaneously with dedicated A/D converters at 50kHz along with a synchronization signal whose leading edge was placed temporally in the middle of the PIV pulses. The acoustic pressure signals were phase and amplitude corrected in post processing.

2.4. Operating conditions

The combustor rig was allowed at least 10 minutes to stabilize thermally prior to measurements. The operating conditions are listed in Table 1, and summarized as follows: combustor pressures of $\bar{p}_{comb} \cong 1, 3,$ and 5bar; preheat air temperature measured in the plenum, $T_{pl} \cong 310\text{-}370\text{C}$; thermal power $P_{th}/\bar{p}_{comb} \cong 36\text{kW}/\text{bar}$; ER = 0.69; fuel H₂ volume fraction from 0 to 50% in 10% increments. Note that the ER in cases 1 and 4 was 0.71 to prevent flame blowout. In case 4, the flame blew out at ER = 0.69 due to excessive thermoacoustic oscillations. Furthermore, T_{pl} was maintained to within about 10 degrees for the 3 and 5bar cases (see Table 1). Due to the reduced mass flow rate of the 1 bar cases, in order to avoid damage to the electric heater, the preheat temperature was reduced for those cases by approximately 40K and was more difficult to control. The air mass flow rates, \dot{m}_{air} , and the swirler nozzle average exit velocity, U_0 , are also listed. The 10 and 20% H₂ cases at 1 bar were not achievable as the H₂ flow was too low for stable operation of the mass flow controller. Reynolds number here is based on D_0 , U_0 , and the reactant mixture viscosity at 1, 3 and 5bar was about 3×10^4 , 8×10^4 , and 1×10^5 . The rig exit acoustic boundary condition was pressure

release for 1bar, and choked with 3 and 5bar. Another acoustically relevant parameter is the combustor exit Mach number, $M_{comb,e}$. Isentropic flow equations are used with the further assumptions of constant pressure across the combustor and constant pressure from the nozzle exit to the pressure probe in the rig exhaust section. As the exit nozzle is water-cooled, significant heat loss occurs in reacting cases, and the isentropic assumption may lead to an over-prediction of $M_{comb,e}$. Therefore, $M_{comb,e}$ is < 0.40 to 0.50 for reacting cases, and $\cong 0.25$ for non-reacting cases.

Table 1. Operating conditions: combustor pressure, \bar{p}_{comb} , air temperature in the plenum, T_{pl} , air mass flow rate, \dot{m}_{air} , fuel/air equivalence ratio, ER, %H₂ in fuel by volume, and combustor inlet nozzle average axial velocity, V_0 . At 1bar 10 and 20% fuel H₂ volume fractions could not be reached due to the minimum limit of the H₂ mass flow meter.

Case	\bar{p}_{comb} [bar]	T_{pl} [C]	\dot{m}_{air} [g/s]	ER	H ₂ in fuel [% vol.]	V_0 [m/s]	$\overline{Q}/\bar{p}_{comb}$ [kW/bar]
1	1.06	334	17.6	0.71	0	50.5	35.0
2	1.06	330	17.3	0.69	30	50.4	35.1
3	1.06	317	17.2	0.69	40	49.5	35.1
4	1.05	317	17.0	0.71	50	49.6	35.1
5	0.99	312	17.6	0	No fuel	48.5	0
6	3.07	370	55.2	0.69	0	57.7	36.1
7	3.07	366	55.0	0.69	10	57.4	36.2
8	3.05	368	54.6	0.69	20	58.0	36.4
9	3.04	365	54.1	0.69	30	57.7	36.5
10	3.05	363	53.7	0.69	40	57.5	36.4
11	3.03	363	53.1	0.69	50	57.9	36.6
12	2.99	352	55.2	0	No fuel	53.8	0
13	5.08	360	92.2	0.69	0	57.4	36.4
14	5.04	367	91.7	0.69	10	58.4	36.7
15	5.06	364	91.1	0.69	20	57.9	36.6
16	5.00	371	90.4	0.69	30	59.2	37.0
17	5.01	369	89.5	0.69	40	58.8	36.9
18	4.95	371	88.4	0.69	50	59.7	37.4
19	5.10	360	92.2	0	No fuel	53.3	0

3. Flame topology, hydrodynamics (PVC/HV), and thermoacoustic response

3.1. Flame topology

The flow field topology and a typical flame configuration are sketched in Figure 1. The swirling flow exhibits vortex breakdown with an IRZ and an outer recirculation zone (ORZ) [11,17-25]. Although the

centerbody is tapered, at the current swirl number (about 1.0) the flow separates along the centerbody as observed indirectly from the PIV velocity field [11,17-18,21-25] and matched by LES for the atmospheric burner [19-20], resulting in a conical shear layer [11,17-25]. This inner shear layer (ISL) provides a flame stabilization location. As the ISL is separated for a significant fraction of the centerbody length, ISL stabilized flames are recessed upstream of the dump plane, as evidenced by heat discoloration pattern along the centerbody [11,17-18,21-25] and seen in LES [19-20]. An outer shear layer (OSL) originates from the outer annulus lip and along with the ORZ serves as a secondary flame stabilization location. The flame nominally attaches to the ISL, supported by the IRZ of hot exhaust corresponding to a V-flame. When the flame cannot withstand the hydrodynamic strain in the ISL, for the current flame temperature, heat loss, and fuel composition, the flame detaches partially from the ISL and is aided by a helical shedding vortex. This aerodynamically stabilized flame shape is referred to M.

Figure 3 shows the time-averaged OH* CL for all cases. The V-flame for case 13, 5bar, 0% H₂, matches the flame shape from previous work [22-23], although T_{pl} , \dot{m}_{air} , and ER are similar but not identical there, and D_e is 33 instead of 18mm. Without H₂ enrichment, the effect of pressure is seen by scanning up the first column. An M-flame at 1bar transitions to the familiar V-flame with increased pressure.

Furthermore, the flame shortens in the higher pressure cases. However, as the pressure increases, the Re and correspondingly the turbulence intensity increase, and the heat loss changes, and, therefore, multiple effects are present. The flame length, L_f , scales with the product of average velocity, U_0 , and chemical time, τ_{chem} , $L_f \propto U_0 \cdot \tau_{chem}$. As U_0 changes very little between cases, we may conclude that τ_{chem} is the dominant parameter for flame length.

With H₂ enrichment the M-flame passes through a bi-stable state on the way to a V-flame, and the V-flame is observed to shorten. We refer to the bi-stable flame as V* (see dashed line square in Figure 3). Stabilization in ISL, and hence the V-flame, is possible with the resulting faster chemistry and increased flame extinction stretch rate with H₂ enrichment.

3.2. PVC/HV

The PVC structure dynamics may be detected in the acoustic pressure or PIV data. In this experiment the PVC frequency peak is only seen in the acoustic pressure spectra in its most energetic form with the M-flames (see Figure 5a). We will revisit this point later. In this burner the most identifiable visual feature of the PVC structure is the associated frequency-locked single HV along the ISL. Prominent HVs may sometimes be directly observed in the raw Mie scattering images [15-16] or in the PIV velocity data. The HV appears in planar cut data as staggered counter-rotating vortices along either edge of the conical ISL. However, when turbulence intensity and other dynamic modes are significant modal decomposition is necessary to reveal the PVC structure dynamics. Proper orthogonal decomposition (POD) separates dynamic data into orthogonal modes ordered by decreasing energy, i.e. the lowest order mode is the most energetic. POD on the PIV data is used to separate the HV structure and dynamics from the acoustic modes and turbulence [11,18,23]. In this experiment the HV is isolated by the first two POD modes for all the 3 and 5bar reacting cases, and for the M-flames at 1bar, as well as the non-reacting cases at 1 and 5bar (cases 1-2 and 5-18). The POD mode pairs corresponding to the HV are shown for cases 1, 13, and 18 in Figure 4 for the axial velocity, V . In the remaining cases the HV is spread among multiple POD modes, but the PVC frequency can still be identified. The HV in these cases could be isolated using spectral POD [13, 30-31], but presently for simplicity we exclude those cases from the later discussion on PVC energy. ***The PVC structure exists in all reacting cases with M- and V-flames, and in all non-reacting cases.*** This contrasts previous studies with the PRECCINSTA burner at atmospheric pressure, with non-preheated reactants and thermal powers up to 35kW [15,24-25], in which the PVC/HV only existed in conjunction with the M-flame and was totally suppressed in the V-flame cases. The elevated pressure facility uses preheated air (320-370C vs. 20C) and is geometrically different, potentially changing the density gradient in the wave maker region (the separating ISL from the center body). Namely, the combustor section is longer (200mm vs. 114mm), the cross section is smaller ($80\times 80\text{mm}^2$ vs. $85\times 85\text{mm}^2$), and the exhaust exit diameter is smaller (18mm vs. 40mm). The combination of the rig-specific heat loss and the preheat temperature would affect the reactants to products density ratio. The geometric changes result in different inlet dump and exhaust area ratios, as well as different combustor length-to-height or aspect ratios, all of which, especially the dump ratio, could affect the shear layers and swirling flow characteristics.

The PVC frequency, f_{PVC} for consistency with the previous literature [11,18,23-25], is identified from the associated POD temporal modes, and is not discernible in higher POD modes. Spectra of the first POD temporal mode ensemble-averaged to a 40Hz resolution for cases 1, 3 and 18 are plotted in Figure 5 in dotted lines. For a fixed geometry and flame and flow topology f_{PVC} has been shown to scale with velocity independently of Re [8,10,17-18,24-25]. Namely, f_{PVC} can be reduced using a velocity scaling by computing the Strouhal number, $Sr = f_{PVC}D_0/V_0$. Sr is plotted for all cases in Figure 6a. Non-reacting PVC Sr range from 0.65-0.70. For a given flame shape, across pressure (and Re), ***Sr is nearly constant around 0.78 for the V- and V*-flames, and around 0.70 for the M-flame.*** The M- and V-flames are associated with different flow field and density topologies [11,15-17], as the heat release distribution modifies IRZ/ORZ sizes, centerline recirculation strength, and ISL/OSL development, and therefore PVC dynamics. The value from the previous data [22-23] with a V-flame with the larger D_e (lower exhaust contraction), and at different operating conditions is 0.87. Studies with the atmospheric pressure PRECCINSTA burner [18,24-25], reported non-reacting Sr values of 0.78, and 0.93 with the M-flame. The significant difference in Sr may be due to the geometrical differences between plenums and confinement chambers of the atmospheric- and elevated-pressure burners as outlined above, as the length scaling parameter, D_0 , does not capture the full geometry.

We characterize the PVC structure energy by the total mean kinetic energy per unit mass (half of the square of velocity) in the associated POD mode pair for the M-flames at 1bar and the V-flames at 3 and 5bar. Figure 6b plots the PVC structure energy and distinguishes among non-reacting conditions, V-, V*- and M-flames. ***The M-flame supports a relatively strong PVC, and the V- and V*-flames a much weaker one.*** The PVC with the M-flame is about 5× more energetic than with the V-flame, illustrating significant but not total suppression with heat release in the ISL. Figure 6b indicates that H₂ enrichment from 0 to 50% with the V-flame mildly reduces the PVC energy by about 10%.

3.3. Thermoacoustic response

Before we present thermoacoustic instability operational space maps, we need to discuss the combustor pressure and integrated heat release spectra, and identify relevant parameters and how to interpret them.

Integrated heat release, \dot{Q} , was obtained in a manner like in Moeck, et al. [32]. The OH* chemiluminescence signal was first summed over the entire combustor area to reflect global heat release and second, over half of the combustor area on the side where the pressure sensor is mounted in order to capture the antisymmetric dynamics expected with a PVC. It was verified that the thermoacoustic fluctuations were present in both the full and masked signals, confirming that the dominant thermoacoustic dynamics are axisymmetric.

Therefore, only the half-combustor or masked signal is used in the analysis to enable PVC treatment. Figure 5 plots representative spectra of combustor pressure, p_{comb} , in solid lines, and integrated heat release, \dot{Q} , in dashed lines, for three cases: (a) case 1, $\bar{p}_{comb}=1.05\text{bar}$, 0% H₂, (b) case 13, $\bar{p}_{comb}=5.08\text{bar}$, 0% H₂, and (c) case 18, $\bar{p}_{comb}=4.95\text{bar}$, 50% H₂. The spectra are normalized by the peak value for each case and ensemble-averaged to 10Hz frequency resolution for pressure, and 20Hz for \dot{Q} . The pressure spectrum in (a) has two relatively broad peaks near 400Hz, illustrating that closely spaced acoustic modes exist in this combustor. The heat release is coupled predominantly with the first peak, and weakly with the second. Intermittent thermoacoustics and associated broadened peaks are observed here, as the instability frequency jumps and the amplitude is unsteady. In comparison with (a), the pressure and heat release peaks are much sharper in (b), and somewhat better defined in (c). We name the frequency associated with this first, Helmholtz, thermoacoustic mode, f_1 . Weaker secondary pressure and heat release peaks are sometimes also seen. Note that the H₂-enriched case in (c) shows a higher thermoacoustic mode near 1900Hz, with higher amplitude than at f_1 . Lastly, the first POD mode spectra in dotted lines reveal that f_{PVC} in the M-flame case in (a) (and the other M-flame case, not in the figure) coincides with peaks in the pressure and heat release spectra, but not so in the V-flame cases in (b) and (c). Although the heat release spectra in Figure 5 are from half of the burner in order to reveal antisymmetric dynamics, the PVC peak still shows up with similar amplitude in heat release spectra for the entire combustor area. This suggests that the PVC and heat release are coupling, which is uncommon [8,10]. The PVC structure is possibly coupling with the non-axisymmetric heat release [33]. Swirl burners typically show azimuthal asymmetry, which can be seen in this burner by comparing the two halves of time-averaged OH* CL in Figure 3. The heat release and PVC strength could also be coupling through ER fluctuations [34] as PVC strength decreases in response to increasing heat release.

Though multiple thermoacoustic modes are present, we will focus the rest of the discussion on how H₂ enrichment affects the thermoacoustic response on the lowest, Helmholtz, thermoacoustic mode and associated frequency, f_1 . The combustor thermoacoustic response is described using three measurement quantities:

- (1) RMS combustor pressure, $p_{comb,RMS}$, to reflect the overall sound pressure;
- (2) combustor pressure spectral density at the first thermoacoustic frequency, $\%P_{comb}(f_1)$, to reflect the acoustic pressure amplitude associated with f_1 ; and
- (3) lowest thermoacoustic frequency, f_1 .

The RMS and spectral density values are normalized by the time-averaged combustor pressure, \bar{p}_{comb} , as $\%p_{comb,RMS}/\bar{p}_{comb}$ and $\%P_{comb}(f_1)/\bar{p}_{comb}$. Figure 7 plots isocontours of (1)-(3) in subplots (a)-(c). Starting with the sound pressure in Figure 7a, the highest value is about 0.9% of \bar{p}_{comb} , for case 3 at 1bar and 40% H₂. The other 1bar cases with different H₂ enrichment levels are significantly quieter. With H₂ enrichment the sound pressure in the 3bar cases monotonically decreases, while increasing in the 5bar cases. The $\%P_{comb}(f_1)/\bar{p}_{comb}$ trends in Figure 7b are different than the $\%p_{comb,RMS}/\bar{p}_{comb}$ trends in Figure 7a as the active modes and energy distribution change with combustor pressure and H₂ enrichment (see Figure 4). The trend in the 1bar cases is similar, but the decreasing trend in the 3bar cases is more pronounced, and the trend in the 5bar cases is reversed and is now decreasing. This is significant as combustor hardware may be sensitive to frequency in addition to sound pressure. Lastly, Figure 7c shows that H₂ enrichment monotonically increases f_1 . The combustor thermoacoustic response presented in Figure 7 will be analyzed in the following section.

4. Thermoacoustic response analysis

This section discusses how H₂ enrichment affects the thermoacoustic frequency and amplitude. We examine the details of how H₂ enrichment modifies the relative phasing between the acoustic pressure and heat release, which determines how the acoustic pressure and the heat release interact.

4.1. Thermoacoustic frequency scaling

The thermoacoustic frequency is determined by the natural frequency of the active acoustic mode of the system. The present combustor system behaves as a network of Helmholtz resonators as the large combustor

and plenum volumes join via the small swirler passage volume (see Figure 1). The rig sections after the combustor exit nozzle may also be acoustically significant, especially for NR cases, which have lower $M_{comb,e}$. Furthermore, the rig acoustic exit boundary condition changes with pressure from pressure release at 1bar to choked at 3 and 5bar. The natural frequency of a Helmholtz resonator is given by $f_H = 1/2\pi C \cdot c$, where C is a constant determined by the geometry and c is the sound speed. Therefore, the natural frequency of a particular mode is expected to scale with a reference sound speed. In order to check whether a sound speed based on the measured plenum temperature or combustor adiabatic temperature captures the thermoacoustic frequency variation, Figure 8 plots in (a) f_1 vs. a combustor adiabatic product temperature sound speed, c_{comb} , and in (b) f_1 vs. a plenum temperature sound speed, c_{pl} . V-flames and V*-flame are denoted with filled and M-flames with empty symbols. f_1 and c_{comb} in Figure 8a are strongly linearly correlated for the 3 and 5bar cases, while the 1bar cases are clear outliers. To highlight this, a line is fitted to the 3 and 5bar cases.

When f_1 and c_{pl} are related in Figure 8b, all cases strongly linearly correlate, but the V*- and V-flames follow one scaling, while the M-flames a different one. Again for clarity, a line is fitted to the V*- and V-flames. The M-flame thermoacoustic frequencies being lower than with the V-flame may be explained by the flame shapes. Referencing Figure 2, the ISL stabilized V-flames should produce higher average swirler passage and combustor temperatures than the aerodynamically stabilized M-flames. As described previously, due to the ISL being separated from the centerbody for a significant fraction of the centerbody length, the V-flames are recessed upstream of the dump plane. This results in a higher swirler passage average temperature, and higher sound speed. In contrast the M-flames are stood-off from the dump plane. The unburnt reactant mixture reaches further than with a V-flame, resulting in lower swirler passage average temperature, and lower combustor average temperature. The elevated swirler passage temperature is supported by the difference in centerbody temperature, measured with a thermocouple within the center body, 5.5mm from the tip: ~300C for M-flames, and ~450C for V*- and V-flames at 1bar. We conclude that *the plenum sound speed is useful as a reference parameter for the thermoacoustic frequency, with different scaling for V- and M-flames*. Since the sound speed captures both T_{pl} and H₂ enrichment effects, it

can be used to compare different cases. Isocontours of c_{pl} are plotted in Figure 8c to be used for cross-referencing.

4.2. On thermoacoustic amplitude

4.2.1. Governing physics

As previously discussed, in this facility with the PRECCISTA burner, mass flow rate fluctuations in response to the Helmholtz acoustics are transported convectively from the plenum through the swirler to the flame front and equivalence ratio fluctuations from the swirler to the flame. The relative phasing of the acoustic pressure and the heat release fluctuation would determine whether positive feedback exists in the thermoacoustic cycle. This is expressed by the Rayleigh criterion:

$$\int_V p' \dot{q}' dV > 0 \quad \text{Eq. 1}$$

where p' is pressure per unit volume and \dot{q}' is heat release rate per unit volume. This inequality implies that if the p' and \dot{q}' phases are within 90 degrees the system may be thermoacoustically unstable. If the system is thermoacoustically unstable the pressure and heat release phases must be within 90 degrees. In this section we model how the pressure/heat release phase difference for the Rayleigh criterion is determined by relating the travel time of the Helmholtz acoustics pressure wave to H_2 enrichment and plenum temperature.

Figure 9 illustrates the geometry of this process as the pressure wave begins its cycle at $t_{0,p}$ in the plenum. We note that the Helmholtz pressure wave travels much slower than the sound speed. After a time interval $\Delta t_{pl,sw}$, at time t_{dump} it has reached the dump plane, $x = 0$. Next it enters the combustor and propagates further until it reaches the flame at t_f . We define the flame location, $x = L_f$, as the point of maximum RMS heat release, $\max(\dot{q}'_{RMS})$. Identification of this location from the OH* CL images will be shown in the next section.

Figure 10 illustrates the evolution of the pressure and the heat release fluctuations by plotting notional amplitudes in time at the flame location, $x = L_f$. The heat release cycle begins at $t_{0,\dot{q}}$. Following a time-interval Δt_p , at $t_{0,p}$ the pressure cycle begins. As illustrated in Figure 9, the pressure wave must travel through the plenum and swirler over $\Delta t_{pl,sw}$ to the dump plane, enter the combustor, and then reach the

flame location, $x = L_f$, over Δt_f . After the heat release peaks at $t_{360,\dot{Q}}$, following the pressure wave delay time Δt_p the pressure cycle ends at $t_{360,p}$.

The phase difference between the pressure and the heat release for the Rayleigh criterion are determined by Δt_p , as the pressure delay time relative to the integrated heat release. The pressure phase delay angle is defined as:

$$|\varphi_{\dot{Q}} - \varphi_p|_{x=L_f} = 360^\circ \cdot \Delta t_p / T_{TA} \quad \text{Eq. 2}$$

Thus the thermoacoustic period can be expressed as the sum of the pressure travel time intervals:

$$T_{TA} = \Delta t_p + \Delta t_{pl,sw} + \Delta t_f \quad \text{Eq. 3}$$

Now that the pressure travel delay times are related, the times can be expressed as phase delay angles over the thermoacoustic period, reducing the number of parameters in Eq. 3 by one:

$$360^\circ = 360^\circ \cdot (\Delta t_p + \Delta t_{pl,sw} + \Delta t_f) / T_{TA} \quad \text{Eq. 4}$$

or:

$$360^\circ = \Delta\varphi_p + \Delta\varphi_{pl,sw} + \Delta\varphi_f \quad \text{Eq. 5}$$

4.2.2. Governing parameters

Due to the unsteady turbulent nature of the flow there will be variation from cycle to cycle, and, therefore, time-averaged values are used for the phase angles in Eq. 5. Next, the pressure phase delay angle, $\varphi_{\dot{Q}} - \varphi_p$, is computed from the pressure and integrated heat release measurements. As indicated in Figure 9, the combustor pressure, p_{comb} , is measured at the dump plane, and the pressure phase increases over the time interval, Δt_f , required to reach the flame position, $x = L_f$. Therefore the pressure measurement needs to be time shifted according to the relation:

$$|\varphi_p(t)|_{x=L_f} = |\varphi_p(t - \Delta t_f)|_{x=0} \quad \text{Eq. 6}$$

The incremental propagation time for the travelling acoustic pressure wave is given by:

$$dt = \frac{dx}{v_\varphi(x)} \quad \text{Eq. 7}$$

where v_ϕ is the phase velocity. Integrating as the pressure wave passes from the dump plane to the flame, we obtain:

$$\Delta t_f = \int_{t_{dump}}^{t_f} dt = \int_0^{L_f} \frac{1}{v_\phi(x)} dx \quad \text{Eq. 8}$$

This requires obtaining L_f and v_ϕ . The point of maximum RMS heat release or $x = L_f$ is extracted from RMS (and time-averaged) CL images, assuming axial symmetry. The time-averaged images are first Abel-deconvolved [35] to produce a radial-axial time-averaged heat release distribution. The resulting mapping is used to Abel-deconvolve the RMS images, which are then multiplied by r to transform the RMS heat release into physical space. Figure 11 shows the location of maximum RMS heat release obtained from such images for two cases: case 13 in (a), and case 18 in (b). The M-flame in case 1 is long and very near to the combustor sidewall, and its intensity drops suddenly at the wall. Therefore, L_f could not be extracted for this case.

The pressure wave phase speed is the speed of a point at a particular phase, or $v_\phi = |dx/dt|_{\phi=const.}$. First the axial velocity, V , along the jet centreline is extracted as a function of x and t , as in Figure 12. Then v_ϕ as the pressure wave translates from the dump plane to the flame is given by the slope of the locus of points of constant phase. $v_\phi(x)$ is computed for each case by taking the average over all available cycles. Now Δt_f is evaluated using Eq. 8. Figure 13 plots Δt_f vs. L_f and shows that Δt_f has a non-linear dependence on L_f . When the flame is compact the high heat release density locally accelerates the gas flow along annular jet. This effect diminishes with longer flames, and therefore, Δt_f increases faster than linearly with L_f .

Finally, the dump plane pressure measurement is phase-corrected using Eq. 6, and Δt_p is extracted from the pressure and integrated heat release signals. Following Eq. 2, the pressure phase delay angle, $\phi_{\dot{q}} - \phi_p$, is computed at f_1 . Next the thermoacoustic amplitude sensitivity to $\phi_{\dot{q}} - \phi_p$ is examined. Figure 14 plots the pressure spectral density at the thermoacoustic frequency, $P(f_1)$, vs. the pressure phase delay angle, $\phi_{\dot{q}} - \phi_p$. The V-flame cases are shown with filled symbols, and the one available M-flame with an empty symbol. ***The pressure phase delay angle varies from about -40 to 60°, and the thermoacoustic amplitude at f_1 sharply peaks around 0 deg.*** This is in accordance with the Rayleigh criterion.

Next, we investigate how H₂ enrichment determines, $\Delta\varphi_{pl,sw}$, $\Delta\varphi_f$, and eventually the pressure phase delay angle, $\Delta\varphi_p$. For a given case, $\Delta\varphi_f$ and $\Delta\varphi_p$ are obtained from measurements, and according to Eq. 5, the balance to 360° yields $\Delta\varphi_{pl,sw}$. It was determined earlier that the sound speed in the plenum, c_{pl} , is a reference parameter for the thermoacoustic frequency or period, T_{TA} , as it captures both plenum temperature, T_{pl} , and H₂ enrichment effects. Figure 15 plots $\Delta\varphi_{pl,sw}$, $\Delta\varphi_f$, and $\Delta\varphi_p$ vs. c_{pl} with overlaid linear fits. The M-flame is pointed out. Starting with $\Delta\varphi_{pl,sw}$, we note the downward sloping linear trend. With Helmholtz resonance $\Delta t_{pl,sw}$ and f_H are linearly related. Given the dependence of f_H on a reference sound speed, i.e. c_{pl} , therefore, $\Delta\varphi_{pl,sw}$ depends on c_{pl} . The $\Delta t_{pl,sw}$ dependence on f_H can be explained as follows. The gas velocity amplitude inside the Helmholtz cavity and throat increases linearly with f_H , as the gas must move faster to cover the same displacement in a shorter time. As the gas velocity increases, $\Delta t_{pl,sw}$ decreases. The phase delay angle from the dump plane to the flame, $\Delta\varphi_f$, shows its own smooth decreasing trend (generally non-linear) with c_{pl} , determined by the complex interplay of the flame chemistry and the flow field as discussed earlier. Since $\Delta\varphi_{conv}$ is the balance to 360°, after the sum of two downward trending parameters, $\Delta\varphi_p$ trends upward. In the discussed trends, two 1bar cases are outliers in Figure 15: the M-flame in case 2, and the V-flame corresponding to $c_{pl} = 499\text{m/s}$ in case 4 (see Table 1). Both of these cases have different sound speed distributions relative to the other flames in Figure 15. For the M-flame this was previously attributed to the different associated temperature field. The V-flame in case 4 is at a higher ER=0.71 relative to ER=0.69 for the rest of the cases.

The combustor stability model sensitivity to T_{pl} and H₂ enrichment, or what is considered a significant change in operating conditions, can be defined based on the scatter of $\Delta\varphi_p$ as follows. The maximum deviation of the data from the $\Delta\varphi_p$ line excluding the outlier cases 1 and 4 corresponds to an uncertainty in $\Delta\varphi_p$ of $\pm 20^\circ$. Based on the line slope, this corresponds to an uncertainty in c_{pl} , $\epsilon_{c_{pl}} = \pm 6\text{m/s}$. Within the range of the operating conditions (see Table 1) this $\epsilon_{c_{pl}}$ corresponds approximately to an uncertainty in T_{pl} , $\epsilon_{T_{pl}} = \pm 15\text{C}$, and a 0 to 30% H₂ enrichment. These equivalencies were determined by calculating the change in reactant sound speed with changing reactant temperature and composition.

In summary a simple thermoacoustics model was used to understand and interpret the effects of plenum temperature and H₂ enrichment on the thermoacoustic amplitude. The thermoacoustic frequency increases as plenum temperature and H₂ enrichment raise the sound speed. In Helmholtz resonance the pressure wave travel time in the plenum and swirler passage drops with the frequency. H₂ enrichment and plenum temperature shorten the flame and decrease the travel time required to reach the flame. The balance between the thermoacoustic period and the total travel time to the flame determines the phase difference between the pressure and heat release fluctuations, and therefore, controls the thermoacoustic amplitude. Therefore, ***plenum temperature and H₂ enrichment increase the pressure phase delay angle relative to the heat release.***

4.2.3. Capturing thermoacoustic amplitude trends within the operating space

With the help of the reference parameter, c_{pl} , in Figure 8b, and the trends of the Eq. 5 parameters in Figure 15, the trends in Figure 7b can now be explained. To demonstrate, we start at 1bar, picking the 40% H₂ case 3, which has the highest thermoacoustic amplitude at 1bar. We call this point A and denote it in Figure 7b, Figure 8c, and Figure 15. According to Figure 8c c_{pl} is about 495m/s. We reference Figure 15 and focus on the variation of $\Delta\varphi_{conv}$ with c_{pl} . We note that the pressure phase delay, $\Delta\varphi_{conv}$, is nearly zero, and any significant changes to c_{pl} ($\epsilon_{c_{pl}} = \pm 6\text{m/s}$) would drive $\Delta\varphi_{conv}$ away from zero, reducing the thermoacoustic amplitude. This matches the observations in Figure 7b that increasing or decreasing the H₂ enrichment reduces the thermoacoustic amplitude. Since H₂ enrichment and T_{pl} both drive c_{pl} up, this means not only that changing H₂ enrichment decreases the thermoacoustic amplitude, as seen in Figure 7b, but also that changing T_{pl} would have the same effect.

We pick another point, point B, as the 3bar, 10% H₂ case 7 this time with intermediate thermoacoustic amplitude. Point B is also denoted in Figure 7b, Figure 8c, and Figure 15. Referencing Figure 8c c_{pl} is about 507m/s, and $\Delta\varphi_p$ is around 20° from Figure 15. Now the trend in Figure 15 predicts that increasing c_{pl} will only increase $\Delta\varphi_p$ bringing it farther away from 0. Therefore, increasing H₂ enrichment and T_{pl} will reduce the thermoacoustic amplitude. In contrast, decreasing H₂ enrichment and T_{pl} will increase the thermoacoustic

amplitude until a maximum is reached at $\Delta\varphi_p = 0$ with a corresponding $c_{pl} = 499\text{m/s}$. Again, the observations in Figure 7b are matched.

Finally, the pressure phase delay data referenced to the plenum sound speed, c_{pl} , can now be used to predict the effect of H_2 enrichment and T_{pl} on the thermoacoustic amplitude at untested operating points within the present range of operating conditions (see Table 1). Thus a predicted stability map in T_{pl} vs. $\% \text{H}_2$ enrichment space can be constructed, and such a map plotted in Figure 16. The ranges of T_{pl} and $\% \text{H}_2$ match their ranges in Table 1. Isocontours of the reference parameter, c_{pl} , are computed from T_{pl} and the fuel composition corresponding to $\% \text{H}_2$ and plotted in Figure 16 with a reference line for $c_{pl} = 499\text{m/s}$, corresponding to $\Delta\varphi_p = 0$ (see Figure 15), the theoretical maximum thermoacoustic amplitude. The farther away the operating conditions are from the $\Delta\varphi_p = 0$ isoline, the lower the thermoacoustic amplitude would be. For example, points such as $T_{pl} = 620\text{C}$, $\% \text{H}_2 = 5$, and $T_{pl} = 610\text{C}$, $\% \text{H}_2 = 25$, are predicted to have relatively high thermoacoustic amplitudes, while points such as $T_{pl} = 595\text{C}$, $\% \text{H}_2 = 5$, and $T_{pl} = 645\text{C}$, $\% \text{H}_2 = 45$, are predicted to have lower thermoacoustic amplitudes. Points A and B from the previous discussion are also overlaid in Figure 16, showing that the high thermoacoustic amplitude point A is near the $\Delta\varphi_p = 0$ isoline, while the lower amplitude point B is farther away.

Concluding remarks

The effect of H_2 enrichment on the flame shape, precessing vortex core (PVC) structure characteristics, and thermoacoustic frequency and amplitude for a gas turbine model combustor at elevated pressure were examined. H_2 enrichment shortens the flame through faster chemistry, and causes an aerodynamically stabilized M-flame to transition to a shear layer stabilized V-flame, when the flame can withstand the hydrodynamic strain in the shear layer. The PVC/HV was observed with both flame shapes. In contrast studies with the same injector geometry but different plenum and confinement at atmospheric pressure and with non-preheated air, found that the PVC/HV was completely suppressed with the V-flame. In the present study the velocity fluctuations associated with the HV are $10\times$ higher for the M-flame, and monotonically decrease with H_2 enrichment for both flame shapes ($6\times$ from 0 to 50% H_2 with the V-flame). Furthermore Sr is around 0.78 for the V-flame, and is notably lower (around 0.70) for the M-flame.

A simple model for the convective coupling between the Helmholtz acoustics and the heat release rate was used to explain and interpret the effects of H₂ enrichment on the thermoacoustic frequency and amplitude. In the experiment the plenum temperature was lower at 1 bar, and H₂ enrichment was varied at each pressure. The effect of H₂ enrichment and plenum temperature on the thermoacoustic frequency and amplitude is captured by the sound speed in the plenum.

Increasing H₂ enrichment and plenum temperature increases the thermoacoustic frequency. The strength of the positive thermoacoustic feedback depends on the phase delay between the pressure and heat release. The pressure phase delay was expressed as the balance between the thermoacoustic period and the total pressure wave travel time from the plenum to the flame location. Using the sound speed reference parameter and the thermoacoustic model, it was shown that increasing H₂ enrichment and the plenum temperature increased the pressure phase delay through two effects. One was to decrease the pressure wave travel time from the plenum to the dump plane with increasing frequency. The second was to decrease the travel time from the dump plane to the flame as a combination of a shortened flame with an increased associated pressure wave speed. Thus the thermoacoustic amplitude variation across operating conditions was explained. For cases with a negative pressure phase delay, increasing H₂ enrichment and/or plenum temperature increased the thermoacoustic amplitude, while decreasing it for cases with a positive phase delay. For cases in which the pressure and heat release were in phase, any change to H₂ enrichment or plenum temperature would decrease the thermoacoustic amplitude. The effect of simultaneous changes to H₂ enrichment and plenum temperature can be explained by using the plenum sound speed reference parameter. The uncertainty of the predictions was estimated using the data spread as 15C for the plenum temperature and 20-30% H₂ volume in the fuel.

Acknowledgements

This project has received funding from the European Research Council (ERC) under the European Union's Horizon 2020 research and innovation programme (Grant agreement No. 682383).

References

- [1] T. Lieuwen, V. McDonell, D. Santavicca, T. Sattelmayer, Burner development and operability issues associated with steady flowing syngas fired combustors, *Combust. Sci. Technol.* 180 (2008) 1169-1192.
- [2] S.J. Shanbhogue, Y.S. Sanusi, S. Taamallah, M.A. Habib, E.M.A. Mokheimer, A.F. Ghoniem, Flame macrostructures, combustion instability and extinction strain scaling in swirl-stabilized premixed CH₄/H₂ combustion, *Combust. Flame* 163 (2016) 494-507.
- [3] A.F. Ghoniem, A. Annaswamy, S. Park, Z.C. Sobhani, Stability and emissions control using air injection and H₂ addition in premixed combustion, *Proc. Combust. Inst.* 30 (2005) 1765-1773.
- [4] Q. Zhang, D.R. Noble, T. Lieuwen, Characterization of fuel composition effects in H₂/CO/CH₄ mixtures upon lean blowout, *J. Eng. Gas Turb. Power* 129 (2007) 688-694.
- [5] T. Lieuwen, V. McDonell, E. Petersen, D. Santavicca, Fuel flexibility influences on premixed combustor blowout, flashback, autoignition, and stability, *J. Eng. Gas Turb. Power* 130 (2008) 011506.
- [6] M. Emadi, D. Karkow, T. Salameh, A. Gohil, A. Ratner, Flame structure changes resulting from hydrogen-enrichment and pressurization for low-swirl premixed methane-air flames, *Int. J. Hydrogen En.* 37 (2012) 10397-10404.
- [7] R.W. Schefer, D.M. Wicksall, A.K. Agrawal, Combustion of hydrogen-enriched methane in a lean premixed swirl-stabilized burner, *Proc. Combust. Inst.* 29 (2002) 843-851.
- [8] N. Syred. A review of oscillation mechanisms and the role of the precessing vortex core (PVC) in swirl combustion systems, *Prog. En. Combust. Sci.* 32 (2006) 93-161.
- [9] C.E. Cala, E. Fernandes, M.V. Heitor, S.I. Shtork, Coherent structures in unsteady swirling jet flow, *Exp. Fluids* 40 (2006) 267-276.
- [10] H. Liang, T. Maxworthy, An experimental investigation of swirling jets, *J. of Fluid Mechanics* 525 (2005) 115.

- [11] S. Terhaar, K. Oberleithner, C.O. Paschereit, Key parameters governing the precessing vortex core in reacting flows: An experimental and analytical study, *Proc. Combust. Inst.* 35 (2015) 3347-3354.
- [12] Q. An, A.M. Steinberg, The role of strain rate, local extinction, and hydrodynamic instability on transition between attached and lifted swirl flames, *Combust. Flame* 199 (2019) 267-278.
- [13] K. Manoharan, M. Frederick, S. Clees, J. O'Connor, S. Hemchandra, A weakly nonlinear analysis of the precessing vortex core oscillation in a variable swirl turbulent round jet, *J. Fluid Mechanics* 884 (2020).
- [14] M. Arnab, N. Muthichur, C. More, S. Gupta, S. Hemchandra, The role of the centerbody wake on the precessing vortex core dynamics of a swirl nozzle, *ASME Turboexpo paper GT2020-15777* (to appear in *J. propulsion and power*).
- [15] I. Chterev, B. Emerson, T. Lieuwen, Velocity and stretch characteristics at the leading edge of an aerodynamically stabilized flame, *Combust. Flame*, 193 (2018) 92-111.
- [16] I. Chterev, C.W. Foley, D. Foti, S. Kostka, A.W. Caswell, N. Jiang, A. Lynch, D.R. Noble, S. Menon, J.M. Seitzman, T.C. Lieuwen, Flame and flow topologies in an annular swirling flow, *Combust. Sci. Technol.* 186 (2014) 1041-1074.
- [17] K. Oberleithner, S. Terhaar, L. Rukes, C.O. Paschereit, An investigation on dynamic characteristics of a gas turbine rotor using an improved transfer matrix method, *J. Eng. Gas Turb. Power* 135 (2013).
- [18] K. Oberleithner, M. Stöhr, S.H. Im, C.M. Arndt, A.M. Steinberg, Formation and flame-induced suppression of the precessing vortex core in a swirl combustor: experiments and linear stability analysis, *Combust. Flame* 162 (2015) 3100-3114.
- [19] W. Meier, P. Weigand, X.R. Duan, R. Giezendanner-Thoben, Detailed characterization of the dynamics of thermoacoustic pulsations in a lean premixed swirl flame, *Combust. Flame* 150 (2007) 2-26.
- [20] B. Fiorina, R. Vicquelin, P. Auzillon, N. Darabiha, O. Gicquel, D. Veynante, A filtered tabulated chemistry model for LES of premixed combustion, *Combust. Flame* 157 (2010) 465-475.
- [21] P. Wang, N.A. Platova, J. Fröhlich, U. Maas, Large eddy simulation of the PRECCINSTA burner, *Int. J. Heat Mass Transfer* 70 (2014) 486-495.
- [22] C.D. Slabaugh, I. Boxx, S. Werner, R.P. Lucht, W. Meier, Structure and dynamics of premixed swirl flames at elevated power density, *AIAA J.* 54 (2016) 946-961.

- [23] R. Zhang, I. Boxx, W. Meier, C.D. Slabaugh, Coupled interactions of a helical precessing vortex core and the central recirculation bubble in a swirl flame at elevated power density, *Combust. Flame* 202 (2019) 119-131.
- [24] A.M. Steinberg, C.M. Arndt, W. Meier, Parametric study of vortex structures and their dynamics in swirl-stabilized combustion, *Proc. Combust. Inst.* 34 (2013) 3117-3125.
- [25] A.M. Steinberg, I. Boxx, M. Stöhr, C.D. Carter, W. Meier, Flow-flame interactions causing acoustically coupled heat release fluctuations in a thermo-acoustically unstable gas turbine model combustor, *Combust. Flame* 157 (2010) 2250-2266.
- [26] Stöhr, M., Z. Yin, and W. Meier. Interaction between velocity fluctuations and equivalence ratio fluctuations during thermoacoustic oscillations in a partially premixed swirl combustor. *Proc. Combust. Inst.* 36 (2017) 3907-3915.
- [27] N. Docquier, S. Candel, Combustion control and sensors: a review, *Prog. En. Combust. Sci* 28 (2002) 107-150.
- [28] J.G. Lee, D.A. Santavicca, Experimental diagnostics for the study of combustion instabilities in lean premixed combustors, *J. Propuls. Power* 19 (2003) 735-750.
- [29] Y. Hardalupas, M. Orain, Local measurement of the time-dependent heat release rate and equivalence ratio using chemiluminescence emissions from a flame, *Combust. Flame* 139 (2004) 188-207.
- [30] A. Towne, O.T. Schmidt, T. Colonius, Spectral proper orthogonal decomposition and its relationship to dynamic mode decomposition and resolvent analysis, *J. Fluid Mechanics* 847 (2018) 821-867.
- [31] M. Sieber, C.O. Paschereit, K. Oberleithner, Spectral proper orthogonal decomposition, *J. Fluid Mechanics* 792 (2016) 798-828.
- [32] J.P. Moeck, J.F. Bourgoin, D. Durox, T. Schuller, S. Candel, Nonlinear interaction between a precessing vortex core and acoustic oscillations in a turbulent swirling flame, *Combust. Flame* 159 (2012) 2650-2668.
- [33] F. Lückoff, K. Oberleithner, Excitation of the precessing vortex core by active flow control to suppress thermoacoustic instabilities in swirl flames, *Int. J. Spray Combust. Dynamics* 11 (2019) 1756827719856237.

[34] Shreekrishna, S. Hemchandra, T. Lieuwen, Premixed flame response to equivalence ratio perturbations, *Combustion Theory Modelling* 14 (2010) 681-714.

[35] C.J. Dasch, One-dimensional tomography: a comparison of Abel, onion-peeling, and filtered backprojection methods, *Applied Optics* 31 (1992) 1146-1152.

Figures

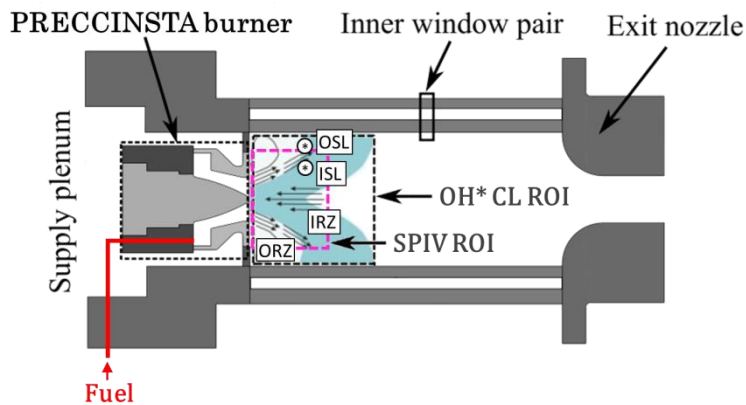


Figure 1. PRECCINSTA premixed swirl burner [22-23]. The flame and flow topology are sketched. The stereo PIV and OH* CL fields of view are indicated.

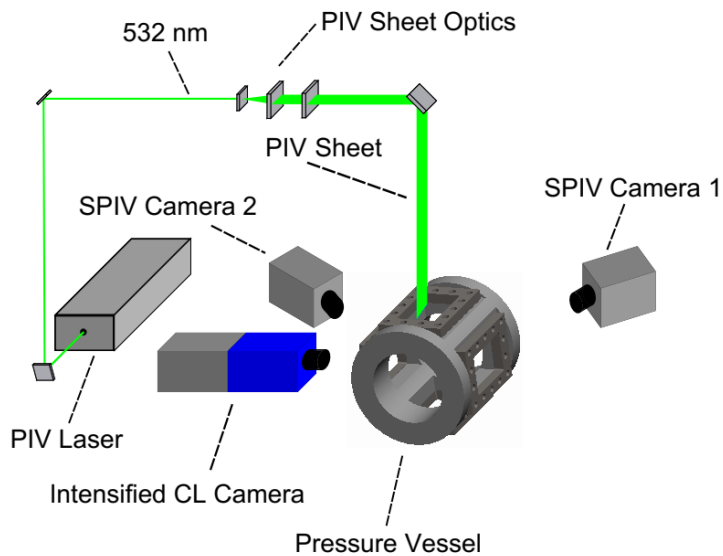


Figure 2. Schematic of simultaneous stereo PIV and OH* chemiluminescence [22-23].

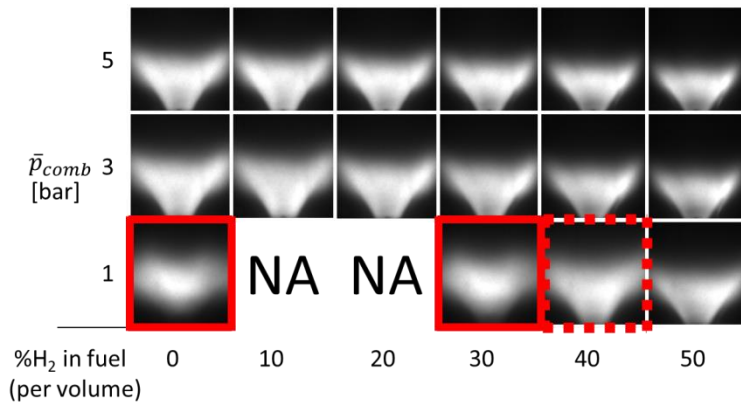


Figure 3. Flame shapes as combustor pressure vs. %H₂ in fuel by volume. M-flames are highlighted in solid lines, and the transitional V*-flame in dashed lines. At 1bar the 10 and 20% H₂ cases were not achievable due to the minimum flow rate capability of the H₂ mass flow meter.

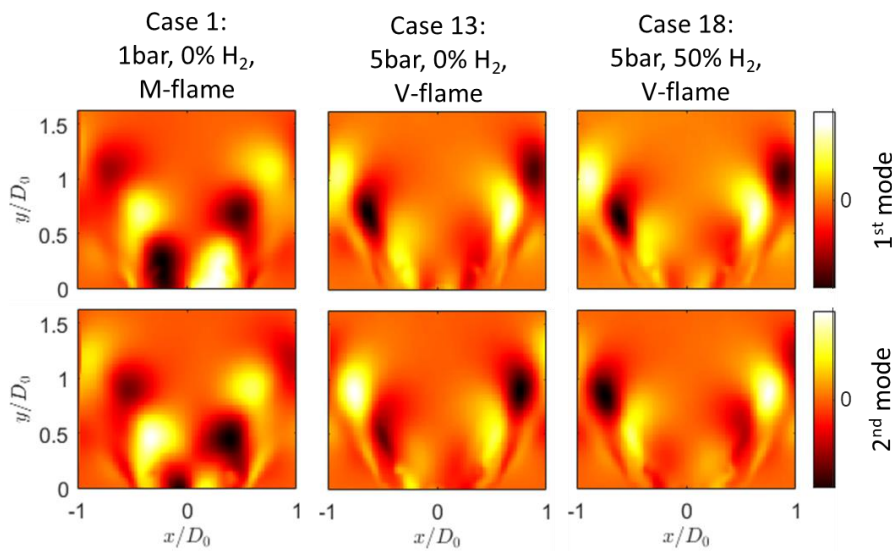


Figure 4. PVC structure 1st/2nd POD mode pair for cases 1, 13 and 18. Axial velocity, V , shown.

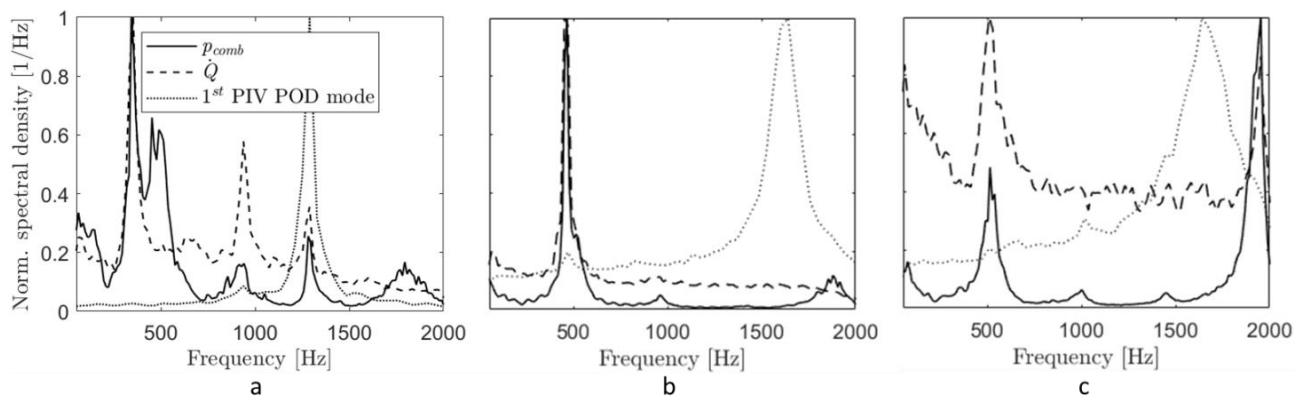


Figure 5. Combustor pressure, integrated heat release, and 1st PIV POD temporal mode (PVC) spectra at three operating conditions: (a) case 1, $\bar{p}_{comb}=1.05\text{bar}$, 0% H₂ by volume in fuel; (b) case 13, $\bar{p}_{comb}=5.08\text{bar}$, 0% H₂; (c) case 18, $\bar{p}_{comb}=4.95\text{bar}$, 50% H₂.

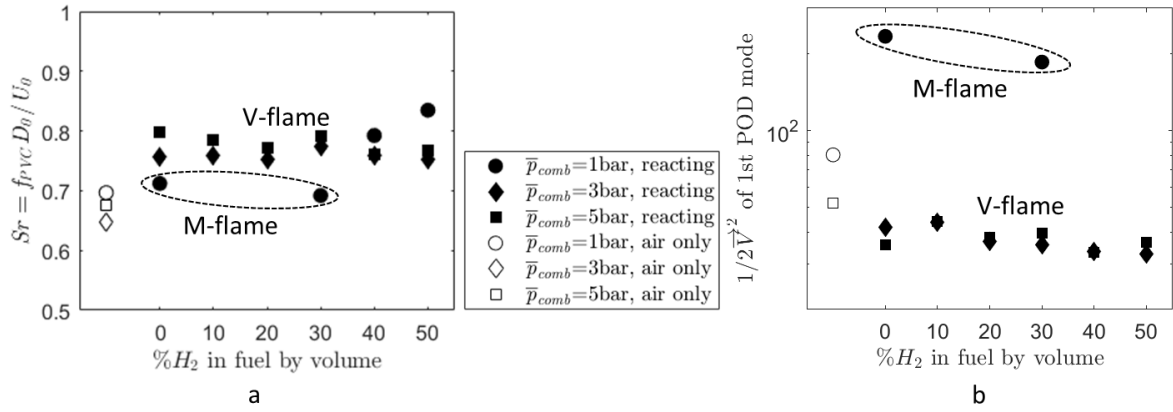


Figure 6. (a) Precessing vortex core (PVC) Strouhal number, Sr . (b) PVC structure energy (total mean kinetic energy per unit mass in associated POD mode pair).

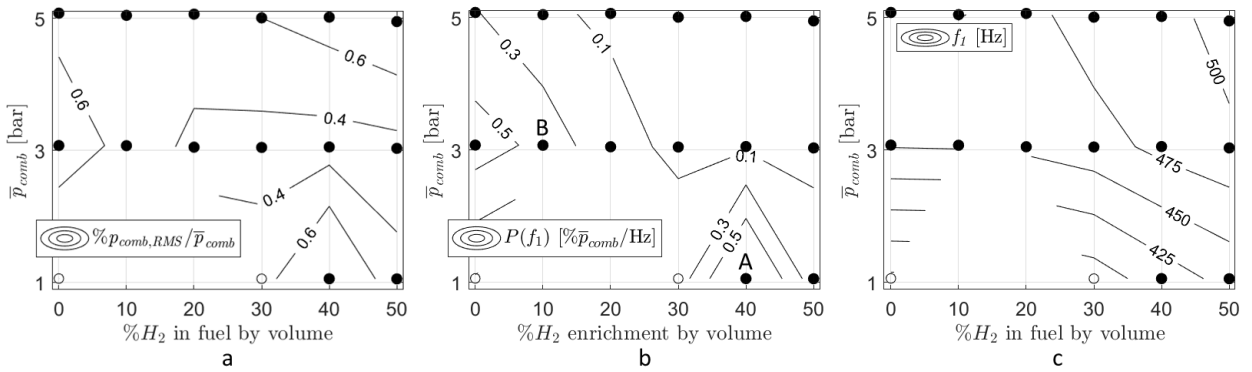


Figure 7. Operability maps as a function of combustor pressure, \bar{p}_{comb} , and $\%H_2$ in fuel by volume. Empty symbols denote M-flames, and solid symbols denote V-flames: (a) RMS combustor pressure, $p_{comb,RMS}$, (b) combustor pressure spectral density at the thermoacoustic frequency, $P(f_1)$, (c) thermoacoustic frequency.

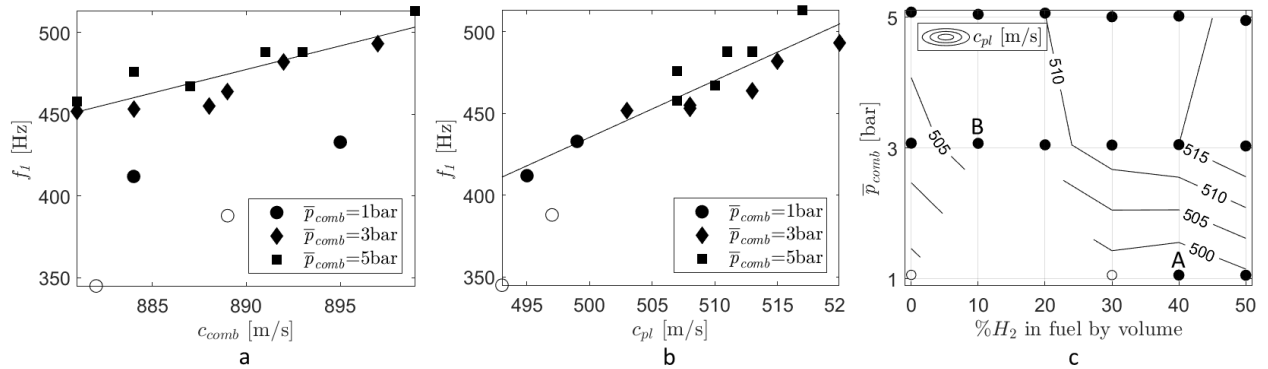


Figure 8. Sound speed reference temperature for thermoacoustic frequency, f_1 , scaling. Solid symbols are V-flames, empty symbols are M-flames. (a) sound speed assuming adiabatic equilibrium products, c_{comb} , (b) plenum sound speed, c_{pl} , (c) plenum sound speed as function of combustor pressure, \bar{p}_{comb} , and H_2 enrichment as a cross-reference parameter.

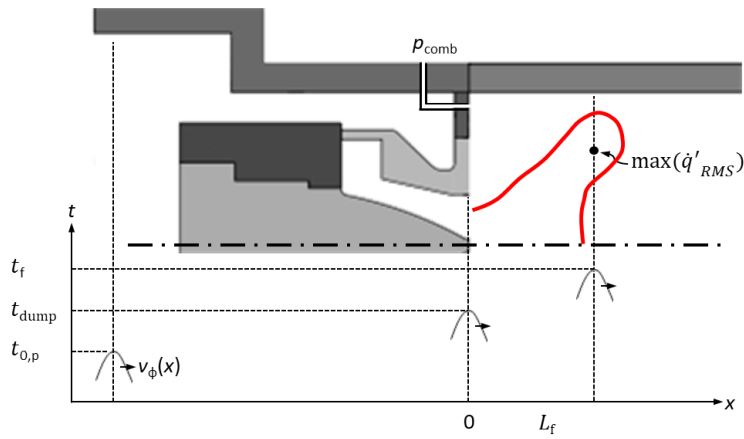


Figure 9. Propagation of the pressure wave through the plenum, swirler and combustor.

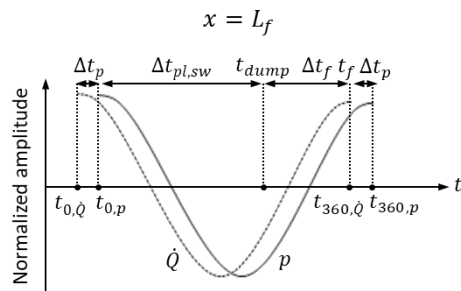


Figure 10. Pressure and heat release cycles at the flame location.

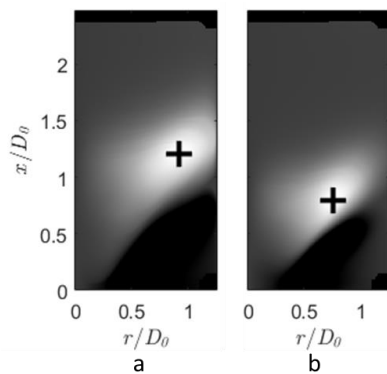


Figure 11. Identification of the point of maximum RMS heat release from Abel deconvolved RMS OH* chemiluminescence images. The image intensity is multiplied by r to represent the RMS heat release distribution in a thin polar slice. (a) case 13, (b) case 18.

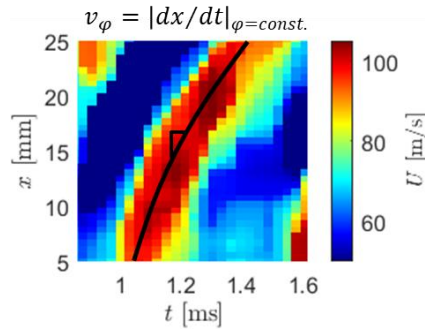


Figure 12. Travelling acoustic wave phase velocity, v_ϕ , extraction from PIV data. Axial velocity, V , along the jet centerline is plotted on axial position vs. time coordinates. The slope of the locus of V at constant phase is averaged over all available cycles to yield the phase velocity.

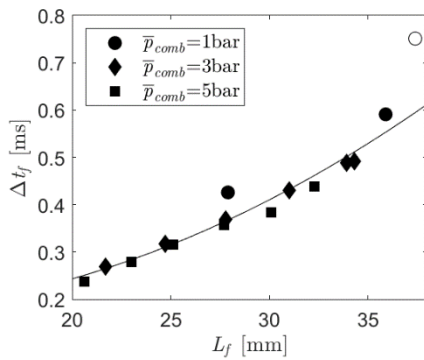


Figure 13. Dependence of the pressure wave travel time from the dump plane to the flame on flame length. Solid symbols are V-flames, empty symbol is the M-flame.

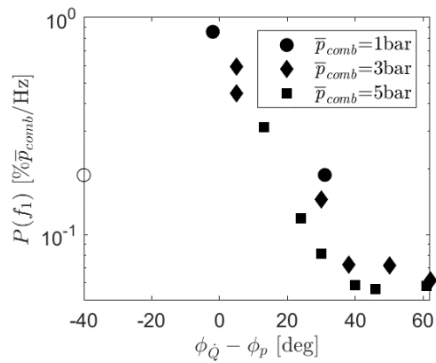


Figure 14. Combustor pressure spectral density at the thermoacoustic frequency vs. the pressure phase angle delay relative to heat release. Solid symbols are V-flames, empty symbol is the available M-flame.

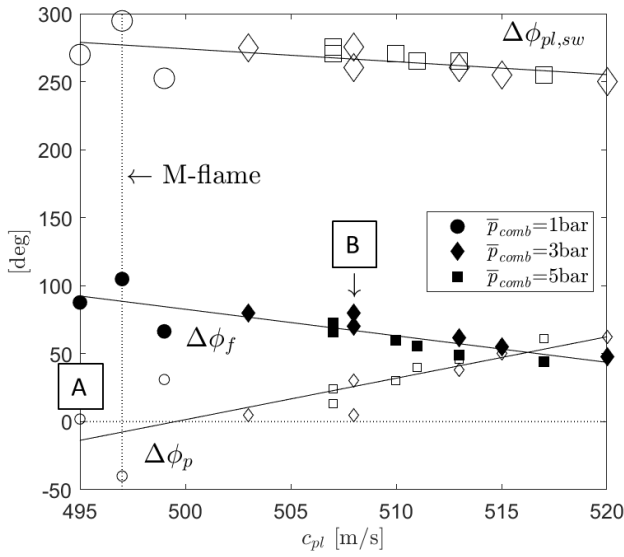


Figure 15. Pressure wave phase delay angles from Eq. 5: from the plenum to the dump plane, $\Delta\phi_{pl,sw}$; from the dump plane to the flame, $\Delta\phi_f$; and for the pressure relative to the heat release, $\Delta\phi_p$.

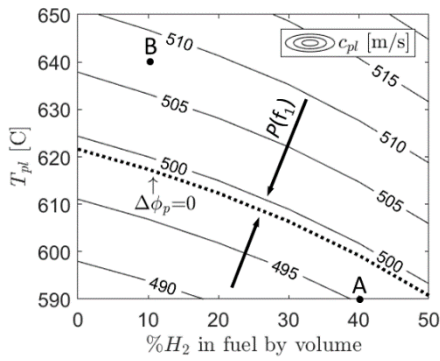


Figure 16. Predicted thermoacoustic stability map in T_{pl} vs. $\%H_2$ enrichment space, constructed using the reference parameter of plenum sound speed, c_{pl} , and Figure 15. The trends of increasing thermoacoustic amplitude are indicated with arrows.